Fast imaging of millimeter-scale areas with beam deflection transmission electron microscopy

Zhihao Zheng[1], Christopher S. Own[2], Adrian A. Wanner[1,3], Randal A. Koene[2], Eric W. Hammerschmith[1], William M. Silversmith[1], Nico Kemnitz[1], Ran Lu[1], David W. Tank[1], H. Sebastian Seung[1,†]

[1]Princeton Neuroscience Institute, Princeton University, Princeton, NJ, USA
[2]Voxa, Seattle, WA, USA
[3]Present address: Paul Scherrer Institute, Villigen, Switzerland
[†]Correspondence to sseung@princeton.edu

Abstract

Serial section transmission electron microscopy (TEM) has proven to be one of the leading methods for millimeter-scale 3D imaging of brain tissues at nanoscale resolution. It is important to further improve imaging efficiency to acquire larger and more brain volumes. We report here a three fold increase in the speed of TEM by using a beam deflecting mechanism to enable highly efficient acquisition of multiple image tiles (nine) for each motion of the mechanical stage. For millimeter-scale areas, the duty cycle of imaging doubles to more than 30%, yielding a net average imaging rate of 0.3 gigapixels per second. If fully utilized, an array of beam deflection TEMs should be capable of imaging a dataset of cubic millimeter scale in several weeks.

Introduction

Volume electron microscopy (vEM) is so far the only approach that has ever been used to reconstruct a connectome – a complete map of neural connectivity at synaptic resolution for an entire brain or nervous system[1–4]. In general, vEM can be categorized into scanning electron microscopy (SEM) or transmission electron microscopy (TEM) techniques[5,6], depending on whether the electron beam is raster-scanned over a sample surface or passed through a thin section of the sample. Block face imaging using single-beam SEMs[7,8] has been widely adopted and in the case of focused ion beam SEM (FIB-SEM)[9–11], offers superior axial resolution. However, single-beam imaging, which sequentially scans one pixel at a time, is inefficient and limits the size of the imaged volume. Recent developments of multiple parallel electron beams[12–14] have dramatically increased throughput but necessitated imaging on thin sections or in conjunction with advanced milling technique[15,16].

In principle, TEM has superior imaging efficiency as all electrons are captured simultaneously. However, transmission imaging requires the tissue block to be sliced into consecutive ultra-thin sections, a technique known as serial section TEM (ssTEM). Classically, ssTEM is used for 3D reconstruction of neural tissues at small scale[17–19]. At large scale, cutting and collecting tens of thousands of ultra-thin sections consistently is challenging. Large-scale

imaging with TEM is therefore either laborious or necessitates custom engineering for automation. In the 1980s, ssTEM was used for mapping the connectome of *C. elegans*[1]. Later on, ssTEM was used to acquire 3D EM datasets of multiple *C. elegans*[20,21], an entire fly larval brain[22], normal and pathological retinas[23,24], and mouse cortex[25,26]. Recently, automation and parallelization of TEM[25,27,28] have allowed imaging of ever larger volumes, such as a complete adult fly brain[2] and a cubic millimeter volume of mammalian cortex[29].

The previous state of the art in high throughput TEM was a system at the Allen Institute for Brain Science[27]. This achieves high imaging speed through several innovations. A reel-to-reel tape translation system allows automated delivery of sections based on GridTape technology[28]. A CMOS camera with a 30-megapixel effective frame size and a low distortion lens achieves a burst imaging rate of 0.5 gigapixels per sec (GPix/s). A scalable software infrastructure allows closed-loop workflow management based on real-time image processing[30]. However, imaging time for a cubic millimeter volume is still 6 months with multiple TEMs[27] and there is a growing need to image much larger datasets[3,31].

Constrained by microscope optics, TEM has a relatively small field of view. To image a square millimeter area, it requires thousands of x-y stage translations to acquire image tiles that are later stitched together to form a multi-tile image. Because the time to image a tile has become so fast the stage translations require more time than the image capture itself[27]. A massive number of positional translations – typically ~10,000 per mm^2 – also rapidly consumes piezo stage life of ~10 billion cycles of the crystal per year when operated 24/7. Therefore, to advance the state of the art, it is essential to reduce the overhead due to stage translations.

Deflection of electron beams is widely used in lithography and microscopy to avoid unintended exposure of samples[32–34]. The control and behavior of beam deflection have been carefully examined down to picosecond time scale[35–37]. In comparison, stage movement is often followed by a residual drift and requires a settling time of tens of milliseconds[2,38]. Beam deflection is therefore commonly used to minimize overhead and side effects of stage motion. In structural biology, to capture images of the same structure at many different orientations, beam deflection is used to take a large number of particle images, each at a different, previously unexposed location, all without moving the stage[39–41]. However, to image a large area at millimeter scale and nanoscale resolution, there's a limitation of how far beam deflection can extend. While existing software can combine beam deflection and stage movement to image a large area[42,43], the performance is not sufficient for high-throughput imaging.

Results

A beam deflection mechanism (Cricket™) for high-throughput TEM imaging has been proposed briefly[27]. Here we report the development of a TEM imaging pipeline that integrates beam deflection with state-of-the-art stage, section feed, and camera technologies (Supplementary Fig. 1a), including an automated reel-to-reel tape translation system[27,28] and a CMOS camera with a 36-megapixel frame size[27]. We present quantifications of several key aspects of the system, including imaging speed, quality, capacity, and its application across

resolutions. The bdTEM achieves the fastest TEM imaging rate to date, a three fold increase over the previous TEM with the same camera[27].

Beam deflection (Cricket). We repurposed electromagnetic lens deflectors in the TEMs (Fig. 1a-b). The deflectors above the object plane shift the electron beam over the specimen and simultaneously the deflectors below the object plane precisely de-scans the image back onto the TEM camera. As a result, multiple image tiles (a supertile) can be acquired without stage movement (Fig. 1c), a significant improvement over regular TEMs limited to 1 image tile per stage position . When a matrix of 3 x 3 tiles were used for large-scale imaging, overhead for stage motion is significantly reduced, accounting for only 4% of section imaging time with an additional 6% of Cricket settling time (Fig. 1d, Quantification of imaging rates in Methods). As a result, the proportion of time spent on image acquisition out of total time per section, referred to as the imaging duty cycle, is greatly increased. The imaging duty cycle is 32.9% at a resolution of 3 nm per pixel, and 31% for 4 nm per pixel (Methods), a twofold increase compared to a previous peak performance of 15%[27].

Capacity and image quality of beam deflection. We explore the limit of beam deflection by attempting to acquire a maximal number of subtiles at a magnification of 4 nm per pixel, ensuring that each subtile has sufficient overlap with its four neighboring subtiles for seamless montaging. Notably, a supertile maximally consists of 30 full-size subtiles in a rectangle grid of 6 by 5, or 44 subtiles in a cruciform shape (Fig. 2a), with a size of 36 megapixels per subtile (6,000 x 6,000). At a pixel resolution of 4 nm, the stitched supertile covers an area exceeding 100 µm x 100 µm after subtile overlaps are taken into account (Fig. 2b). The image tiles at the outermost edge are not taken into account because they either are significantly obstructed by a circular boundary within the microscope, or have poor quality due to low beam intensity. Mechanical adjustment of objective aperture didn't affect the extent of the boundary, indicating that the compromised beam intensity is likely to be caused by other microscope components—for example, the objective-lens pole piece. Beam deflection can additionally be used across a range of magnifications, up to 100,000 times with a pixel size of 0.09 nm (Supplementary Fig. 2).

Zoom-in images show that beam deflection causes a reduction in image quality (Fig. 2c). We therefore used signal-to-noise ratio (SNR) as a function of spatial frequency[44] to assess image quality across subtiles quantitatively (Methods). Beam deflection causes a slight decrease of SNRs for tiles located farther away from the center (Fig. 2d). Here factors that affect image quality may include defocus[35], increasing aberration[40], or reduced electron dose. Importantly, the minor reduction of SNRs for 8 deflected tiles in the 3 x 3 configuration have no effect on image stitching (Fig. 3a-f), alignment, and segmentation (Fig. 4, Supplementary video 1-2).

Stage and section transition. The TEMs are integrated with a two-axis piezo-driven stage and a previously reported reel-to-reel tape translation system[27,28]. In previous volume TEM techniques, stage step-and-settle time ranged from under 50 ms to 100 ms for one axis[2,27]. The stage in our TEMs achieves an average motion time of 34 ms and 40 ms respectively on x and y axes (Supplementary Fig. 1b-c), increasing efficiency on the remaining stage motions.

The reel-to-reel tape translation system allows automated section exchange and barcode-based slot identification using GridTape technology[27,28]. GridTape is a tape substrate that has regularly spaced apertures (i.e. slots), each milled with an unique barcode and covered with an electron-translucent film to provide support for a section. The transition to image the next section includes: 1) advance the tape to the next slot based on the barcode; 2) capture low-magnification overview image, which is used to define region-of-interest for subsequent high-resolution imaging; 3) center the electron beam, which could be off center due to lens hysteresis; 4) find the best focus for the current section. Basic software has been implemented to run these steps automatically (Supplementary video 3). With improved imaging efficiency and significantly reduced stage motions, the overhead associated with these section transition steps now constitutes a substantial contribution of the total time, at ~35% (Fig. 1d, Table 1).

Optics. The detector optics of the TEM is upgraded with a compact light-optical lens assembly and a high speed CMOS camera that yields a frame size of 6,000 × 6,000 pixels (or 36 MPix). The sensor sits near the film plane of a conventional TEM (Supplementary Fig. 1a), eliminating the impractical need of an extended vacuum column required by the past generations of large pixel-count detectors[25,27]. The initial dataset was acquired at an exposure time of 120 ms (Fig. 3a-e, Supplementary video 1). Images acquired at an exposure time of 40 ms have lower SNR but sufficient resolution for synapse identification and reconstruction of neuronal morphology (Fig. 3f-g, Supplementary video 2). As a result, the burst imaging rate (0.9 GPix/s, imaging only) of bdTEMs is 1.8 times that of the previous fastest imaging rate[27] (0.5 GPix/s).

Quantification of imaging speed. Overall, these modifications dramatically increase imaging throughput. Acquisition of a 1 mm^2 section takes 8.8 minutes including imaging, stage motion, and section transition (net average imaging rate of 0.3 GPix/s at 3 nm/pix, Table 1, and Supplementary Video 3). The net imaging rate is 3 times the peak imaging rate of the previous fastest TEM at 0.1 GPix/s with the same camera[27]. The previous imaging rate[27] includes overhead for image quality control and post-processing. These functionalities have not yet been integrated into our acquisition software but in principle could be performed during the overhead for acquisition software and section transition. To understand the variation of imaging speeds over continuous imaging of a large number of sections, we measured the section imaging rates across 472 sections in a series (Fig. 1e). The standard deviation of imaging speed is minimal, at ~1.4% of per-section speed, demonstrating the consistency of the TEM system.

Automated serial sectioning. The bdTEM imaging system is equipped with reel-to-reel section feed mechanism, which requires serial ultrathin sections to be cut and collected on GridTape. Previous efforts have modified an Automated Tape-Collecting Ultramicrotome (ATUM)[45] to accommodate the regularly spaced apertures and delicate films in GridTape[27,28]. We have similarly modified an ATUMtome (RMC/Boeckeler) to be compatible with an ultramicrotome (Leica UC7) and GridTape (Supplementary Fig. 3). The hardware and software modifications include: 1) repositioning feed and take-up motors to accommodate the large-size GridTape reel, 2) adding a high-precision, three-axis motorized stage, 3) adding a before-sectioning and an after-sectioning cameras to monitor tape status, in addition to the UC7

camera module, 4) implementing closed-loop control software to synchronize tape movement with cutting, 5) implementing feedback control of water level based on a proportional-integral-derivative principle. After these modifications, we have completed two successful serial sectioning and collection of over 3,000 and 9,000 sections, respectively.

Montaging and reconstruction. We set out to test whether images acquired by the bdTEMs can be montaged into millimeter-size sections and subsequently reconstructed into a 3D EM volume. An EM volume of over 3,000 sections of hippocampus CA3 tissue, each 1 mm^2 in size, have been imaged with bdTEMs. All imaged sections have been stitched, with 10% overlap between supertiles and 15% overlap between subtiles within a supertile (Fig. 3a-e, see Data Availability). Ultrastructural features such as postsynaptic densities and vesicles can be clearly defined (Fig. 3e-f). Small-diameter axons and dendrites can be followed across sections. Two cutout volumes, one imaged at 120 ms exposure time and the other at 40 ms, are aligned and segmented (Fig. 4, Supplementary Video 1-2), using our deep learning-based reconstruction pipeline[46]. Qualitative comparison from these cutouts shows the segmentations from two imaging conditions are similar (Fig. 4d). This is not surprising, given that downsampled images at 8 or 16 nm per pixel have been shown to be adequate for high-quality alignment and segmentation[46,47]. These data demonstrate that sequential sections imaged with the bdTEMs can be assembled into a 3D volume to reconstruct neural morphology and connectivity.

TEM facility. An array of four microscopes have been fully installed in our facility (Supplementary Fig. 4). In general, 1 - 2 microscopes are offline for repairs or allocated for testing and development, while the rest have accumulated many months of consistent imaging time with the exception of filament replacements and routine maintenance. By estimate, if the four bdTEMs are running 24/7, imaging a cubic millimeter will take about a month (Table 1). However, non-stop long-term imaging requires further development of automation software that can handle image quality control, workflow management, image and section databases, and stitching and alignment. A scalable architecture with these functionalities has been developed[30] but needs to be adapted to integrate with bdTEMs.

Discussion

Here we report a substantial increase in TEM imaging speed enabled by beam deflection technology. Beside its technical benefit, this technology is more accessible. Similar to previous effort to automate TEM[27,28], our modifications are based on a retrofitted JEOL 1200EX-II microscope and cost for the entire system (< $500,000) is significantly lower compared to equivalent imaging systems, permitting acquisition of multiple TEMs for an imaging facility (six at the Allen Institute for Brain Science[27] and four at Princeton University). The space requirements for such an imaging array is modest given its productivity, spanning an area of 9.3 meters by 5.6 meters in total for 4 microscopes (Supplementary Fig. 4). The current system, however, requires specialized films on GridTape, which scales linearly in cost with the number of sections (USD $4 - $8 per slot); but improving film-making methods and economies of scale may decrease the cost in the future. While some custom engineering, such as automation of serial sectioning and sample delivery, is needed to implement a connectomics imaging pipeline, beam deflection by itself only makes use of the existing beam shift, image shift deflectors

without needing to re-engineer microscope optics. These deflectors are standard components of TEMs from any manufacturer.

TEM has the advantages of high spatial resolution up to atomic scale and better imaging depth, but suffers from limitation in field of view size. Beside connectomics, our approach of combining beam deflection and fast stage movement can be used in many other TEM applications to expand imaging area or increase imaging speed, including cell biology[48], microbiology[49], clinical pathology[50], and material science[51]. In structural biology, beam deflection has been widely used in cryo-EM[39–41], and more recently, in electron tomography[52,53]. There is, however, a growing need to study the structure and function of macromolecules within the broader context of a biological system, such as a cell[54,55]. Automating beam deflection and stage movement plan will greatly expand the target imaging area.

The examinations of imaging overheads (Fig. 1d) and beam deflection limits (Fig. 2a) points to several avenues of future improvements in raw imaging speed. (1) Computational overhead can be reduced by refactoring frequently used tasks in the acquisition software to low-level programs. (2) The current 15% subtile overlap within a supertile can be further reduced, for example, to 8%[27]. (3) Upgrading the optics with a 100 MPix camera will in principle double the burst imaging rate. (4) We have initially used 3 by 3 subtiles for large-scale imaging since one circumference of subtiles minimally demonstrates the benefits of beam deflection. Adding more subtiles should further increase overall imaging speed but return would be diminished given the proportion of stage movement overhead is already down to 4% of total time, with trade-offs of lower SNRs for the tiles located at the peripheries. (5) Given that downsampled data (for instance, at a pixel size of 8 or 16 nm) have proved to be adequate for high-quality alignment and segmentation[46,47], one potential approach to increase imaging speed per unit area of tissue is to either increase pixel size (i.e. microscope magnification) or further decrease exposure time, with the caveat that the loss in information content be carefully evaluated against groundtruth. In fact, fine alignments of volume cutouts show no difference between images acquired with 120 ms and 40 ms exposure time (Supplementary Video 1-2). Given that alignment quality is a major limiting factor influencing segmentation accuracy[46], imaging at 40 ms exposure time should be sufficient. In ongoing large-scale imaging efforts, we are routinely using exposure time of around 40 ms.

Volume EM is dichotomized into SEM-based and TEM-based methods, and both have been shown to be capable of acquiring petascale datasets (MultiSEM[56] and GridTape-based TEM[29]). Multiple parallel electron beam technology is based on sophisticated innovations of illumination and detection optics[12–14]. On the other hand, the improvements in TEM for large-scale connectomic applications are largely focused on stage mechanics, section delivery, and camera sensor[2,27,28]. The motivation is to automate or improve other components to leverage the inherent parallel imaging capability of the transmission mode. Crucially, both imaging methods currently depend on cutting and collecting a large number of ultrathin sections. Sectioning-related artifacts (folds, cracks, knife marks, etc.) are very common, though automated reconstruction methods that are robust to some defects have been developed[46,47]. Wide-area milling of imaged tissue was recently developed to circumvent ultrathin sectioning[15,16]

263 and, if integrated with a MultiSEM, can potentially scale up connectomic volumes beyond
264 petascale. In addition, the reliability of serial sectioning can be improved by magnetic section
265 collection[57]. For TEM, one proposal to improve reliability of sectioning is to increase the
266 thickness of serial sections, which are then imaged with tomography to recover a finer axial
267 resolution[48,58]. Whether SEM or TEM-based techniques is the method of choice for exascale
268 datasets remains to be determined.
269
270 **Methods**
271 **Sample preparation and sectioning.** All procedures were carried out in accordance with the
272 Institutional Animal Care and Use Committee at Princeton University. Mice (C57BL/6J-Tg(Thy1-
273 GCaMP6f) GP5.3Dkim/J, Jackson Laboratories, 028280) aged 6 months were transcardially
274 perfused with a 4 °C fixative mixture of 2.5% paraformaldehyde and 1.3% glutaraldehyde in
275 0.1M Cacodylate with 2mM $CaCl_2$ pH 7.4. The brain was extracted and post-fixed for 36 hrs at
276 4 °C in the same fixative solution. The perfused brain was subsequently rinsed in 0.1M
277 Cacodylate with 2mM $CaCl_2$ for 1 hr (3 x 20 mins, 4 °C) and 300 µm coronal sections were cut
278 on a Leica Vibratome on ice. Sample blocks were cut out and stained based on a modified
279 reduced osmium (rOTO) protocol with the addition of formamide[29,59]. The tissue blocks were first
280 *en bloc* stained with 8% formamide, 2% osmium tetroxide, 1.5% potassium ferrocyanide for 3
281 hours at room temperature. Subsequently, the samples were immersed in 1%
282 thiocarbohydrazide (TCH, 94 mM) 50 °C for 50 mins, followed by a second step of 2% osmium
283 staining for 3 hours at room temperature. The sample was placed in 1% uranyl acetate
284 overnight at 4 °C, followed by lead aspartate (Walton's, 20 mM lead nitrate in 30 mM aspartate
285 buffer, pH 5.5) at 50 °C for 2 hours. After washed with water (3 x 10 mins, room temperature),
286 samples proceeded through a graded acetonitrile dehydration series[60] (50%, 75%, 90% w/v in
287 acetonitrile, 10 minutes each at 4 °C, then 4 x 10 minutes of 100% acetonitrile at room
288 temperature). After a progressive resin infiltration series (33% resin:acetonitrile, 50%
289 resin:acetonitrile, 66% resin:acetonitrile, 8 hours each at room temperature), the sample was
290 incubated in fresh 100% resin overnight at room temperature and the resin was cured in the
291 oven at 60 °C for at least 48 hrs.
292 GridTape (Luxel Corporation) contains regularly spaced apertures with plastic film
293 substrates for serial sections[27,28]. The films are transparent to electrons, and therefore are
294 compatible with TEM imaging. We combined an automated tape collecting system (ATUMtome,
295 RMC/Boeckeler) and an ultramicrotome (UC7, Leica) to create an automated tape-based
296 sectioning and collection system (Supplementary Fig. 3) for GridTape, based on previous
297 designs[27,28]. Our custom ultramicrotome setup also includes a computer-controlled, high-
298 precision motorized stage, monitoring of temperature and humidity, and three cameras to
299 monitor the collection process. Additionally, we have built closed-loop control software to phase-
300 lock aperture movement with cutting, in order to center sections collected in the apertures on
301 GridTape. After resin embedding, the ultrathin sections were then cut at a nominal thickness of
302 40 nm and automatically collected onto a GridTape.
303
304 **Reel-to-reel translation system and GridStage.** The reel-to-reel translation system and
305 GridStage (Voxa) have been described previously[27]. Briefly, Gridstage Reel comprises three
306 major components: a stage cartridge, a reel storage and delivery system, and an airlock

assembly enabling cartridge loading. A 3D rendering of the GridStage Reel system is shown in Supplementary Fig. 1, attached to a JEOL 1200EX-II microscope chassis. GridStage's two-axis stage cartridge is set to a fixed height to enable the imaging environment to stay the same from section to section as they are delivered into the imaging area by conveyor. Each axis is driven by a precision closed-loop piezo motor. The precision is ~50 nm, and absolute positional accuracy on the sample is typically between 100 - 200 nm. This mechanism positions the sample accurately and reliably within the requirements of montage image overlap reproducibility, even given electron-optical environment variability (e.g. charging and sample morphology changes) of different samples in the volume. The cartridge incorporates an accurate barcode reading and clamping mechanism to precisely position and identify slots on GridTape, with read accuracy greater than 99.9% for a new reel of GridTape. This enables precise tracking of the current tissue section under first-time section imaging or during re-imaging operations. The precision of the GridStage sample ID subsystem supports either sequential or fully random-access sample delivery modes.

The stage has fast responsiveness, with roundtrip communication to the drive system on the order of a few milliseconds, and typical step-and-settle times occurring in under 45 ms (Supplementary Fig. 1b-c). The stage motion time is similar to and slightly improved over a previously reported fast Piezo-driven stage[2]. The distributions of stage motion time are spaced at intervals of 2 ms; this stage motion artifact likely exists during actual imaging. While the reason for this splitting has not been accounted for, this effect has minimal influence on the total imaging time given that the average time is relatively fast. During imaging, an extra 10 ms of settle time is added for each movement to ensure stability. The 10 ms per step was taken into account in the stage movement overhead.

Voxa reels are housed in robotic delivery and take-up conveyor systems connected to the microscope's vacuum, and can accept a GridTape reel with up to 7,500 sections spaced 6 mm apart. A continuously-monitored belt tension meter ensures the GridTape translates within specified operating parameters, and supports safe transit of the samples into and out of the imaging area. The GridStage reel sample delivery system can deliver sequential sections as fast as once every two seconds, for quick survey modes.

Lens assembly and camera. The electron optics of each of our TEM systems consists of a custom phosphor scintillator of 75 mm in diameter, a lens assembly (AMT, NanoSprint50M-AV), and a high speed CMOS camera (XIMEA, CB500MG-CM). The pickup area of 47 x 47 mm on the phosphor screen is near the film plane of the JEOL 1200EX-II TEM and therefore minimizes image distortion at the bottom of the column and matches the nominal magnification setting of the microscope platform. Conveniently, this setup eliminates the need for a lengthened column that previously requires building scaffolds and is impractical for many facilities[2,25,27]. In addition, compared to the previous design of an extended column, the smaller scintillator and compact lens in our TEMs allows good signal-to-noise with lower dose or with shorter exposure times leading to more efficient use of available beam electrons. The CMOS camera has a PCIe interface that supports fast data transfer rates. Overall, the lens and camera supports nominal image acquisition with a frame size of 6,000 x 6,000 pixels at a shortest exposure time of 40 ms. In the future, an upgrade of a 100+ Mpix CMOS camera with backside illumination could potentially lead to another couple-fold increase of imaging rate[27].

TEM imaging. Some components of the TEM systems have been briefly presented before[61]. The beam deflection module (Cricket, Voxa) for TEM has been prototyped previously[27] but not demonstrated for large-scale imaging. For imaging, samples on a GridTape reel are first loaded into the reel housing of the reel-to-reel system (Supplementary Fig. 1a), which is connected with the TEM column vacuum. After loading, the microscope is pumped down to reach the vacuum level of ~1E-7 Torr. Lanthanum hexaboride crystal (LaB_6) filaments were used due to their high electron flux per unit area and a longer lifetime (1,000 hrs or more as opposed to 200 hrs for a tungsten source) reducing downtime needed for filament change. Crucially LaB_6 filaments depend more sensitively on a good vacuum pressure for good stability and lifetime (low 10^{-7} Torr). It typically takes about half a day when loading a new sample reel to pump down the column to the base operating pressure for LaB6. We then increase the high-tension voltage to 120 KV, turn on filament current and then perform alignments on various components of the TEM, following routine technical instructions for TEM operations. These procedures take half a day and only need to be performed after installation of a new filament or loading of a new tape. Calibration of reel-to-reel systems involves tape and tension calibration for reliable translation and barcode reading, which typically takes ~5 minutes and is only done when first loading a reel. Cricket alignment is performed to ensure each sub-tile has sufficient overlap (~15%) with neighboring sub-tiles and that there is minimal distortion across the field between images from different sub-tiles to facilitate efficient stitching and reconstruction. Cricket alignment is usually stable over several months.

The TEMs are compatible with GridTape[28], which has regularly spaced 2 x 1.5 mm^2 apertures in aluminum-coated polyimide tape. Each aperture can be identified by a unique barcode milled on the tape. The tape is coated with a 50 nm-thick film (Luxel Corporation) that spans the apertures and serves as support for sections. The steps to perform before imaging every section include: deliver a new aperture into the field of view using the reel-to-reel system, locate the aperture center using stage algorithmically, find the illumination center of the electron beam (which is often off-center due to magnetic hysteresis from magnification change or change in charge equilibrium state of the new aperture), adjust camera gain control, extract ROI, and autofocus at high magnification. These are done for every aperture with a tissue section, and typically take 2 - 3 minutes per aperture (Table 1). Software (Blade, Voxa Inc.) has been developed that can control the Reel-to-reel system, GridStage, and TEM automatically. The software has lower-level functions that execute each step in the workflow (e.g. travel to a specific aperture in the GridTape reel, move the stage, adjust focus of the TEM). The low-level software supports end-user scripting and control of application-specific microscope workflows via the Blade API supplied to the user. Additionally, the Blade software allows initialization of imaging remote control over IP of all operations and multiple user-defined imaging modes - e.g. continuous batch imaging, re-imaging, and selective or random sampling. In a recent large-scale imaging effort, 55 sections need to be re-imaged for a reel of 1785 sections. The re-imaging rate is therefore 3%.

The acquisition computer for each microscope has an intermediate storage of 16 - 32 TB SSDs via a PCIe card with 4 USB3.0 ports, for ~24 hours of imaged data**.** Each USB port can support up to 10 Gb/s of transfer speed. After caching on the temporary storage on SSD, the data are then transferred via a 10 Gb/s network connection to an on-premise petascale cloud

storage in a separate building. Data transfer is done using CloudFiles (https://github.com/seung-lab/cloud-files).

Quantification of imaging rates. In general, imaging rates (Fig. 1d, Table 1) are computed as the number of pixels that are acquired in a given amount of time to image a section. Burst imaging rates are calculated from the number of pixels in a frame over camera exposure time per frame (6,000 x 6,000 pixels in 40 ms). Section imaging rates are calculated from the total number of pixels of all images (i.e. number of pixels in a tile multiplied by number of tiles) over time, from the first image to the last image of a section acquisition. Sources of overhead for section imaging rates include imaging, stage motion, beam deflection, computational overhead of the acquisition software, and computing basic image statistics (Fig. 1d). Net imaging rates are computed from the same number of pixels as in section imaging rate, including all overhead from section imaging, but additionally includes overhead for section transition (e.g. low-magnification overview of sections on GridTape, ROI extraction, autofocus, beam centering). Effective imaging rates are calculated from the total number of pixels of a montage acquisition with overlap pixels only counted once, over the same overhead as in the net imaging rate. Time for a section acquisition varies from section to section depending on variable computational overhead in the acquisition software. Peak imaging rate is taken from an acquisition with the shortest imaging time. Average transition time is the average taken from 10 consecutive automatic acquisitions.

The distribution of section imaging rates (Fig. 1e) is collected from acquisitions of 472 sections over the course of several days of imaging. Because the section imaging rate is calculated by the total number of pixels divided by time span for a given section, the variability of acquisition time span is directly reflected in the variability of section imaging rates. Each section encapasses 748 supertiles, with a size of approximately 1.9 x 1.2 mm^2. Based on these data, the mean and standard deviation of section imaging rates are, respectively, 397.1 MPix/s and 5.5 MPix/s. The section imaging rates are then multiplied by the total number of pixels (i.e. number of pixels per tile multiplied by the tile count) to calculate the time span for imaging a 1 mm^2 section. Based on these data, the mean and standard deviation of imaging time for a 1 mm^2 section is 6.58 mins and 0.9 mins, respectively. These values are empirically consistent with a typical imaging time for a 1 mm^2 area.

The calculation of stage motion overhead involves the multiplication of the average settling time for the x and y axes (34 ms and 40 ms, respectively, Supplementary Fig. 1c-d), by the total number of x and y movements required for imaging a section. Additionally, an extra 10 ms is added for each movement to cover edge cases and ensure sufficient settle time for stage. The 10 ms is used as an imaging parameter in our regular imaging procedures. A 1 mm^2 section consists of 484 supertiles, including 462 x-axis steps (34 ms per step) and 22 y-axis steps (40 ms per step), with an extra 10 ms per step. The total stage motion time is 21.5 seconds. The fraction of stage motion overhead is therefore 4% out of 8.8 mins (6.6 mins imaging time and 2.2 transition time). Given the standard deviation of x and y stage movements are 1 ms, which is already taken into account in the extra 10 ms (Table 1). The overhead for stage motion for a whole section is therefore quite stable.

Similarly, beam deflection overhead involves multiplication of per-tile settle time by the number of subtiles. We have empirically used a Cricket settle time of 8 ms per subtile. Given

beam deflection operates on the order of several milliseconds or much less[35,36,62], instances of fuzzy images caused by beam deflection are exceedingly rare with 8 ms. The total Cricket settle time for a 1 mm^2 section is therefore 31 seconds (8 ms per subtile, for a total of 484 supertiles, each with 8 beam-deflected subtiles), which represent 6% out of total time per section (8.8 mins).

Overall, the time required for stage motion and beam deflection during the imaging of a section are determined by the total tile count for a section and tends to remain stable. The variances of their fractions are therefore determined by the variances of total section imaging time (Fig. 1e).

Imaging duty cycle is computed as the fraction of time for image acquisition (number of tiles multiplied by exposure time per tile) out of total time per section. For example, at 3 nm/Pixel the image acquisition time is 2.9 minutes (4,356 tiles at 40 ms per tile), which is 32.9% out of total time per section (8.8 minutes). Similarly, the imaging duty cycle at 4 nm/Pixel is 31%. In comparison, the peak performance of the previous state of the art system[27] has an imaging duty cycle of 15% (2,600 tiles at 50 ms per tile out of 14 minutes of total time).

Quantification of signal-to-noise power ratios (SNR). We used a previously described method[44] to determine SNR as a function of spatial frequency for images. Two-dimensional spatial power spectra were computed for each image and collapsed into one dimension by radial averaging. Electron beam was blocked to collect noise images and the power spectra of noise images were computed using the same procedure and subtracted. The magnitude of SNRs are different between Fig. 2d and Fig. 3g, because different magnifications were used (3 vs. 3.6 nm/pix, respectively) and, as a result, the electron doses are different.

Stitching, alignment, and segmentation. Image stitching was performed with the AlignTK software[25] (https://mmbios.pitt.edu/aligntk-home). Image alignment and segmentation was performed with a custom software pipeline[46].

Data availability

Data for 100 sections imaged at 120 ms exposure time are fully stitched and can be accessed in https://neuroglancer-demo.appspot.com with the source precomputed://https://s3-hpcrc.rc.princeton.edu/ca3-aligned-2023/image_cutout. Here for a direct link to the data.

Code availability

Code is available from https://github.com/seung-lab/PyAGTUM

Table 1. Performance metric for bdTEMs.

Supplementary video 1. Aligned images across 55 sections acquired at 120 ms exposure time.

Supplementary video 2. Aligned images across 20 sections acquired at 40 ms exposure time.

Supplementary video 3. Screen recording of an acquisition at a peak imaging rate.

Acknowledgments
The Cricket system was initially prototyped and tested by Voxa with the Allen Institute for Brain Science[27]. We thank R. Clay Reid, Daniel J. Bumbarger, Wenjing Yin, Derrick Brittain, Marc Takeno, Nuno Macarico da Costa, David Hildebrand for advice on microscopy and serial sectioning setup; Stephan Y. Thiberge for help in the planning and construction of the TEM facility; Lawrence Own and Teddy DeRego for their development and support in GridStage and Cricket hardware and software; Wei-Chung Allen Lee and Jasper Phelps for advice on image stitching; John Price for modification of ATUMtome. This work was supported by the NIH grants 1S10OD023602-01A1, 1U19NS104648, 1U19NS132720 and the Simons Collaboration on the Global Brain. The authors acknowledge the use of Princeton's Imaging and Analysis Center, which is partially supported through the Princeton Center for Complex Materials (PCCM), a National Science Foundation (NSF)-MRSEC program (DMR-2011750).

Author contributions
C.S.O. and A.A.W. conceived the study. Z.Z. developed the conceptual framework for quantifying the performance. D.W.T. and H.S.S. acquired funding and supervised. A.A.W. planned the construction of the facility and managed the installation and testing of the first instrument. A.A.W. registered and stitched the initial datasets. Z.Z., C.S.O., and R.A.K. developed software for TEM imaging. Z.Z., A.A.W., and E.W.H. developed software and hardware for serial sectioning. W.M.S. developed software for data transfer. Z.Z. performed image stitching. Z.Z. and N.K. performed image alignment. R.L. performed segmentation. Z.Z. acquired and analyzed data. Z.Z. and C.S.O. carried out validation and evaluation. Z.Z. and H.S.S. drafted the manuscript with input from all authors.

Competing interest
N.K., R.L., and H.S.S. disclose financial interests in Zetta AI LLC. C.S.O. and R.A.K. disclose financial interests in Voxa. A.A.W. is a founder and owner of ariadne.ai ag (Switzerland).

Fig. 1. Beam deflection for TEM imaging.
a, A ray diagram for beam deflection in TEM. **b - c,** Cricket sequentially scans each tile of a 3 x 3 matrix pattern on the sample, producing a "supertile" at a stage position with overlap between tiles. Neighboring supertiles (different colors) can be stitched together to form a montage image. **d**, Imaging speed based on acquisitions at 3 nm/pix (Methods). The bar lengths are proportional to the contribution of overheads to imaging speed. Computational overhead of acquisition ("acq software") includes communications between different components, software time jitters, computing image statistics, on-the-fly stitching of subtiles to supertiles, and writing image files. Effective imaging rates are calculated from the total number of pixels of a montage acquisition with overlap pixels only counted once ("tile overlap"), over the same overhead as in the net imaging rate. Stage movement and Cricket settling times are determined by the number of tiles and generally remain constant for a specific section (Methods). Therefore, the variability in their proportions is determined by the variability in section imaging rate (~1.4%, **e**). **e**, The distribution of section imaging rates for 472 sections. The size of each section is 1.9 x 1.2 mm^2. The

526 average rate is 397.1 MPix/s (s.d. 5.5).
527
528 **Fig. 2. Limit and image quality of beam deflection.**
529 **a**, Maximal number of subtiles imaged with beam deflection in the JEOL 1200EX-II TEM. Each
530 tile has 6,000 x 6,000 pixels with a pixel resolution of 3.6 nm. **b**, A fully stitched montage of the
531 subtiles in (**a)** that are minimally blocked. Each tile and its neighboring tiles have overlap, which
532 is used for the stitching. **c**, Zoom-in images from each of three tiles highlighted in colors (**a)**. **d**,
533 The signal-to-noise ratio (SNR) as a function of spatial frequency (Methods) for each image was
534 computed and shown with colors of the tiles indicated in the legend.
535
536 **Fig. 3. High-throughput millimeter-area imaging with beam deflection.**
537 **a,** A fully stitched montage of a hippocampus section (1 mm^2) imaged with a Cricket-equipped
538 TEM, at a pixel resolution of 3 nm. The montage includes 4320 tiles (or 480 supertiles). **b,** A
539 montage of 6 stitched supertiles (from red outline in **b**). **c,** A Cricket supertile consisting of 9 tiles
540 (from orange outline in **b**). Each tile has 6,000 x 6,000 pixels and the overlap between
541 neighboring subtiles of a supertile is 15% (~900 pixels). **d**, A single image tile (from green
542 outline in **c**). **e,** Further zoom-in shows synaptic vesicles and a cross-section plane of a
543 mitochondria. **f**, Same area and zoom-in as in **e** but imaged with 40 ms exposure time. The
544 whole section is imaged with 120 ms exposure time (**a - e**). **g**, SNRs of the images (**e, f**) are
545 computed with the same procedure as Fig. 2d.
546
547 **Fig. 4. Segmentation of bdTEM imaged data.**
548 Alignment and dense segmentations of two cutout volumes of the same area in hippocampus
549 CA3 region imaged with bdTEM. **a - d**, EM overview and segmentation of a cutout volume
550 imaged with 120 ms exposure time (191 x 151 x 2.48 $\mu m^{3,}$, 55 sections); **e**, An overview
551 showing segmentation of another cutout volume imaged with 40 ms exposure time (191 x 151 x
552 0.9 μm^3, 20 sections).
553
554 **Supplementary Fig. 1. A bdTEM for high-throughput imaging.**
555 **a,** A refurbished JEOL 1200EX-II TEM with 120 KV accelerating voltage. The custom
556 modifications include a beam deflection mechanism (Cricket, Voxa), an advanced reel-to-reel
557 tape translation system with a dual-axis piezo-driven fast stage (GridStage, Voxa), and a high
558 speed CMOS camera (CB500MG-CM, XIMEA) with improved lens design (NanoSprint50M-AV,
559 AMT). **b - c**, Distributions of stage motion time in x (**c**) and y (**d**) axes, with 2,500 counts of
560 measurements for either axis. x-axis, mean 34.18 ms, s.d. 0.97 ms; y-axis, mean 40.09 ms, s.d.
561 1.14 ms. The stage is designed to carry less mass on the x-axis and therefore travels faster in
562 the x direction. During imaging, an extra 10 ms of settling time is added for each movement to
563 ensure stability (Methods). **d,** Overview of a section on a 2 mm x 1.5 mm slot imaged using
564 Cricket at low magnification.
565
566 **Supplementary Fig. 2. High-resolution imaging with bdTEM.**
567 **a - c,** High-resolution electron micrographs of a mouse cortex sample imaged with Cricket. Each
568 of three supertiles are respectively imaged with magnifications of 20,000 (**a**, 0.48 nm/pix),
569 40,000 (**b**, 0.24 nm/pix), and 100,000 (**c**, 0.093 nm/pix) in the JEOL 1200EX-II TEM. A

magnified view of the subtiles located in the upper right corner is shown on the right-hand side.

Supplementary Fig. 3. GridTape compatible automated ultramicrotome.
a - b, A photograph and a 3D model of an ATUMtome (RMC/Boeckeler) modified to be compatible with GridTape and Leica UC7 ultramicrotome. (A), Before-sectioning camera; (B), after-sectioning camera; (C) , UC7 camera module. **c,** Software interface for automated sectioning comprises three modules. Tape control module (left), the video from the before-sectioning camera (A) shows a GridTape aperture with a barcode on the top; the video from the after-sectioning camera (B) shows drying and outline of a section on the film in the aperture. Water-level module (center), the video from UC7 camera (C) shows the light reflection of an ultrathin section (45 nm) on the water, and pixel intensity inside the yellow rectangle is used to provide feedback to monitor water level continuously. Tape stage module (right), software control of a three-axis stage that supports the base plate.

Supplementary Fig. 4. **A bdTEM facility.**
a - b, A floor plan and a photograph of a microscope facility that houses 4 bdTEMs with an inside room for sectioning.

References

1. White, J. G., Southgate, E., Thomson, J. N. & Brenner, S. The structure of the nervous system of the nematode Caenorhabditis elegans. *Philos. Trans. R. Soc. Lond. B Biol. Sci.* **314**, 1–340 (1986).
2. Zheng, Z. *et al.* A Complete Electron Microscopy Volume of the Brain of Adult Drosophila melanogaster. *Cell* **174**, 730–743.e22 (2018).
3. Dorkenwald, S. *et al.* Neuronal wiring diagram of an adult brain. *bioRxiv* (2023) doi:10.1101/2023.06.27.546656.
4. Winding, M. *et al.* The connectome of an insect brain. *Science* **379**, eadd9330 (2023).
5. Peddie, C. J. *et al.* Volume electron microscopy. *Nature Reviews Methods Primers* **2**, 1–23 (2022).
6. Kornfeld, J. & Denk, W. Progress and remaining challenges in high-throughput volume electron microscopy. *Curr. Opin. Neurobiol.* **50**, 261–267 (2018).
7. Leighton, S. B. SEM images of block faces, cut by a miniature microtome within the SEM - a technical note. *Scan. Electron Microsc.* 73–76 (1981).

602 8. Denk, W. & Horstmann, H. Serial block-face scanning electron microscopy to reconstruct
603 three-dimensional tissue nanostructure. *PLoS Biol.* **2**, e329 (2004).
604 9. Heymann, J. A. W. *et al.* Site-specific 3D imaging of cells and tissues with a dual beam
605 microscope. *J. Struct. Biol.* **155**, 63–73 (2006).
606 10. Knott, G., Marchman, H., Wall, D. & Lich, B. Serial section scanning electron microscopy of
607 adult brain tissue using focused ion beam milling. *J. Neurosci.* **28**, 2959–2964 (2008).
608 11. Xu, C. S. *et al.* Enhanced FIB-SEM systems for large-volume 3D imaging. *Elife* **6**, (2017).
609 12. Eberle, A. L. *et al.* High-resolution, high-throughput imaging with a multibeam scanning
610 electron microscope. *J. Microsc.* **259**, 114–120 (2015).
611 13. Mohammadi-Gheidari, A., Hagen, C. W. & Kruit, P. Multibeam scanning electron
612 microscope: experimental results. *J. Vac. Sci. Technol. B Microelectron. Nanometer Struct.*
613 *Process. Meas. Phenom.* **28**, C6G5–C6G10 (2010).
614 14. Ren, Y. & Kruit, P. Transmission electron imaging in the Delft multibeam scanning electron
615 microscope 1. *J. Vac. Sci. Technol. B Nanotechnol. Microelectron.* **34**, 06KF02 (2016).
616 15. Hayworth, K. J. *et al.* Gas cluster ion beam SEM for imaging of large tissue samples with
617 10 nm isotropic resolution. *Nat. Methods* **17**, 68–71 (2020).
618 16. Templier, T. Technologies for Cellular-Resolution Connectomics. (ETH Zurich, 2018).
619 doi:10.3929/ETHZ-B-000267370.
620 17. Harris, K. M. *et al.* Uniform serial sectioning for transmission electron microscopy. *J.*
621 *Neurosci.* **26**, 12101–12103 (2006).
622 18. Stevens, J. K., Davis, T. L., Friedman, N. & Sterling, P. A systematic approach to
623 reconstructing microcircuitry by electron microscopy of serial sections. *Brain Res.* **2**, 265–
624 293 (1980).
625 19. Harris, K. M. & Weinberg, R. J. Ultrastructure of synapses in the mammalian brain. *Cold*
626 *Spring Harb. Perspect. Biol.* **4**, (2012).
627 20. Cook, S. J. *et al.* Whole-animal connectomes of both Caenorhabditis elegans sexes. *Nature*

628 **571**, 63–71 (2019).
629 21. Witvliet, D. *et al.* Connectomes across development reveal principles of brain maturation.
630 *Nature* **596**, 257–261 (2021).
631 22. Eichler, K. *et al.* The complete connectome of a learning and memory centre in an insect
632 brain. *Nature* **548**, 175–182 (2017).
633 23. Sigulinsky, C. L. *et al.* Network Architecture of Gap Junctional Coupling among Parallel
634 Processing Channels in the Mammalian Retina. *J. Neurosci.* **40**, 4483–4511 (2020).
635 24. Pfeiffer, R. L. *et al.* A pathoconnectome of early neurodegeneration: Network changes in
636 retinal degeneration. *Exp. Eye Res.* **199**, 108196 (2020).
637 25. Bock, D. D. *et al.* Network anatomy and in vivo physiology of visual cortical neurons. *Nature*
638 **471**, 177–182 (2011).
639 26. Lee, W.-C. A. *et al.* Anatomy and function of an excitatory network in the visual cortex.
640 *Nature* **532**, 370–374 (2016).
641 27. Yin, W. *et al.* A petascale automated imaging pipeline for mapping neuronal circuits with
642 high-throughput transmission electron microscopy. *Nat. Commun.* **11**, 4949 (2020).
643 28. Phelps, J. S. *et al.* Reconstruction of motor control circuits in adult Drosophila using
644 automated transmission electron microscopy. *Cell* **184**, 759–774.e18 (2021).
645 29. MICrONS Consortium *et al.* Functional connectomics spanning multiple areas of mouse
646 visual cortex. *bioRxiv* 2021.07.28.454025 (2021) doi:10.1101/2021.07.28.454025.
647 30. Mahalingam, G. *et al.* A scalable and modular automated pipeline for stitching of large
648 electron microscopy datasets. *Elife* **11**, (2022).
649 31. Abbott, L. F. *et al.* The mind of a mouse. *Cell* **182**, 1372–1376 (2020).
650 32. Fowler, T. K. & Good, W. M. A theory on obtaining short bursts of ions from a beam of ions.
651 *Nuclear Instruments and Methods* **7**, 245–252 (1960).
652 33. Zhang, L., Hoogenboom, J. P., Cook, B. & Kruit, P. Photoemission sources and beam
653 blankers for ultrafast electron microscopy. *Struct Dyn* **6**, 051501 (2019).

654 34. Auzelyte, V. *et al.* The beam blanking system for microlithography at Lund Nuclear
655 Microprobe. *Nucl. Instrum. Methods Phys. Res. B* **219-220**, 485–489 (2004).
656 35. Zhang, L., Garming, M. W. H., Hoogenboom, J. P. & Kruit, P. Beam displacement and blur
657 caused by fast electron beam deflection. *Ultramicroscopy* **211**, 112925 (2020).
658 36. Gesley, M. An electron optical theory of beam blanking. *Rev. Sci. Instrum.* **64**, 3169–3190
659 (1993).
660 37. Sadorf, H. & Kratz, H. A. Plug-in fast electron beam chopping system. *Rev. Sci. Instrum.*
661 (1985).
662 38. Cheng, A., Tan, Y. Z., Dandey, V. P., Potter, C. S. & Carragher, B. Chapter Four -
663 Strategies for Automated CryoEM Data Collection Using Direct Detectors. in *Methods in*
664 *Enzymology* (ed. Crowther, R. A.) vol. 579 87–102 (Academic Press, 2016).
665 39. Cheng, A. *et al.* High resolution single particle cryo-electron microscopy using beam-image
666 shift. *J. Struct. Biol.* **204**, 270–275 (2018).
667 40. Wu, C., Huang, X., Cheng, J., Zhu, D. & Zhang, X. High-quality, high-throughput cryo-
668 electron microscopy data collection via beam tilt and astigmatism-free beam-image shift. *J.*
669 *Struct. Biol.* **208**, 107396 (2019).
670 41. Weis, F. & Hagen, W. J. H. Combining high throughput and high quality for cryo-electron
671 microscopy data collection. *Acta Crystallogr D Struct Biol* **76**, 724–728 (2020).
672 42. Suloway, C. *et al.* Automated molecular microscopy: the new Leginon system. *J. Struct.*
673 *Biol.* **151**, 41–60 (2005).
674 43. Mastronarde, D. N. Automated electron microscope tomography using robust prediction of
675 specimen movements. *J. Struct. Biol.* **152**, 36–51 (2005).
676 44. Wanner, A. A., Genoud, C., Masudi, T., Siksou, L. & Friedrich, R. W. Dense EM-based
677 reconstruction of the interglomerular projectome in the zebrafish olfactory bulb. *Nat.*
678 *Neurosci.* **19**, 816–825 (2016).
679 45. Hayworth, K. J. *et al.* Imaging ATUM ultrathin section libraries with WaferMapper: a multi-

680 scale approach to EM reconstruction of neural circuits. *Front. Neural Circuits* **8**, 68 (2014).
681 46. Popovych, S. *et al.* Petascale pipeline for precise alignment of images from serial section
682 electron microscopy. *bioRxiv* 2022.03.25.485816 (2022) doi:10.1101/2022.03.25.485816.
683 47. Macrina, T. *et al.* Petascale neural circuit reconstruction: automated methods. *bioRxiv*
684 2021.08.04.455162 (2021) doi:10.1101/2021.08.04.455162.
685 48. Redemann, S. *et al.* C. elegans chromosomes connect to centrosomes by anchoring into
686 the spindle network. *Nat. Commun.* **8**, 15288 (2017).
687 49. Yoshida, N. *et al.* The zebrafish as a novel model for the in vivo study of Toxoplasma gondii
688 replication and interaction with macrophages. *Dis. Model. Mech.* **13**, (2020).
689 50. Erlandson, R. A. CHAPTER 6 - Role of Electron Microscopy in Modern Diagnostic Surgical
690 Pathology. in *Modern Surgical Pathology (Second Edition)* (eds. Weidner, N., Cote, R. J.,
691 Suster, S. & Weiss, L. M.) 71–84 (W.B. Saunders, 2009).
692 51. Ophus, C. Quantitative Scanning Transmission Electron Microscopy for Materials Science:
693 Imaging, Diffraction, Spectroscopy, and Tomography. *Annu. Rev. Mater. Res.* **53**, 105–141
694 (2023).
695 52. Bouvette, J. *et al.* Beam image-shift accelerated data acquisition for near-atomic resolution
696 single-particle cryo-electron tomography. *Nat. Commun.* **12**, 1957 (2021).
697 53. Eisenstein, F. *et al.* Parallel cryo electron tomography on in situ lamellae. *Nat. Methods* **20**,
698 131–138 (2023).
699 54. Elferich, J., Schiroli, G., Scadden, D. T. & Grigorieff, N. Defocus Corrected Large Area
700 Cryo-EM (DeCo-LACE) for label-free detection of molecules across entire cell sections.
701 *Elife* **11**, (2022).
702 55. Lucas, B. A. Visualizing everything, everywhere, all at once: Cryo-EM and the new field of
703 structureomics. *Curr. Opin. Struct. Biol.* **81**, 102620 (2023).
704 56. Shapson-Coe, A. *et al.* A connectomic study of a petascale fragment of human cerebral
705 cortex. Preprint at https://doi.org/10.1101/2021.05.29.446289 (2021).

706 57. Templier, T. MagC, magnetic collection of ultrathin sections for volumetric correlative light
707 and electron microscopy. *Elife* **8**, (2019).
708 58. Soto, G. E. *et al.* Serial section electron tomography: a method for three-dimensional
709 reconstruction of large structures. *Neuroimage* **1**, 230–243 (1994).
710 59. Mikula, S. & Denk, W. High-resolution whole-brain staining for electron microscopic circuit
711 reconstruction. *Nat. Methods* **12**, 541–546 (2015).
712 60. Edwards, H. H., Yeh, Y. Y., Tarnowski, B. I. & Schonbaum, G. R. Acetonitrile as a
713 substitute for ethanol/propylene oxide in tissue processing for transmission electron
714 microscopy: comparison of fine structure and lipid solubility in mouse liver, kidney, and
715 intestine. *Microsc. Res. Tech.* **21**, 39–50 (1992).
716 61. Own, C. S. *et al.* Multi-order Scaling of High-throughput Transmission Electron Microscopy.
717 *Microsc. Microanal.* **25**, 1040–1041 (2019).
718 62. Sadorf, H. & Kratz, H. A. Plug-in fast electron beam chopping system. *Rev. Sci. Instrum.*
719 **56**, 567–571 (1985).

720

Fig. 1

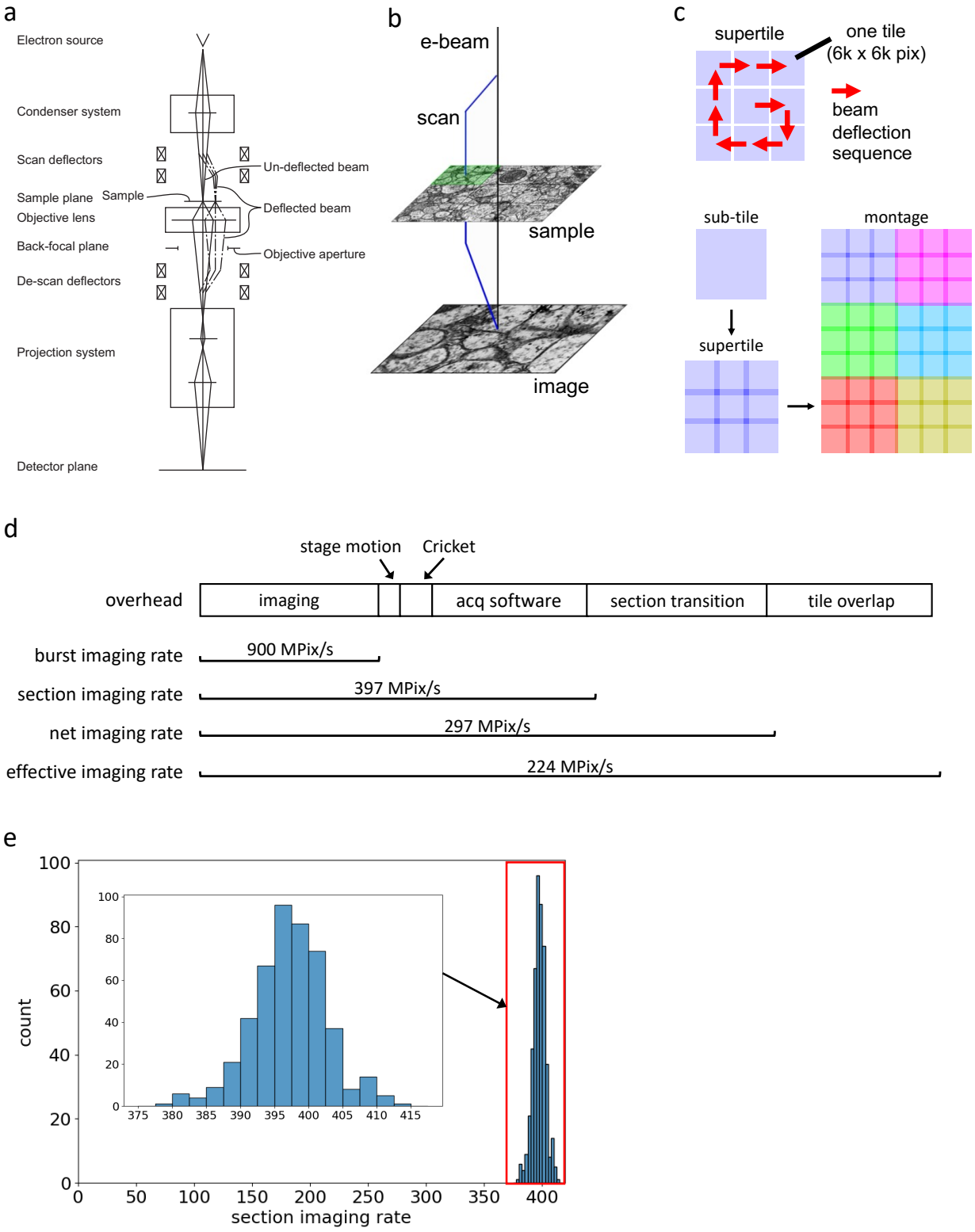
a
Electron source
Condenser system
Scan deflectors
Un-deflected beam
Sample plane
Sample
Deflected beam
Objective lens
Back-focal plane
Objective aperture
De-scan deflectors
Projection system
Detector plane
b
e-beam
scan
sample
image
c
supertile
one tile
(6k x 6k pix)
beam
deflection
sequence
sub-tile
montage
supertile
d
stage motion
Cricket
overhead
imaging
acq software
section transition
tile overlap
burst imaging rate
900 MPix/s
section imaging rate
397 MPix/s
net imaging rate
297 MPix/s
effective imaging rate
224 MPix/s
e
count
section imaging rate

Fig. 2

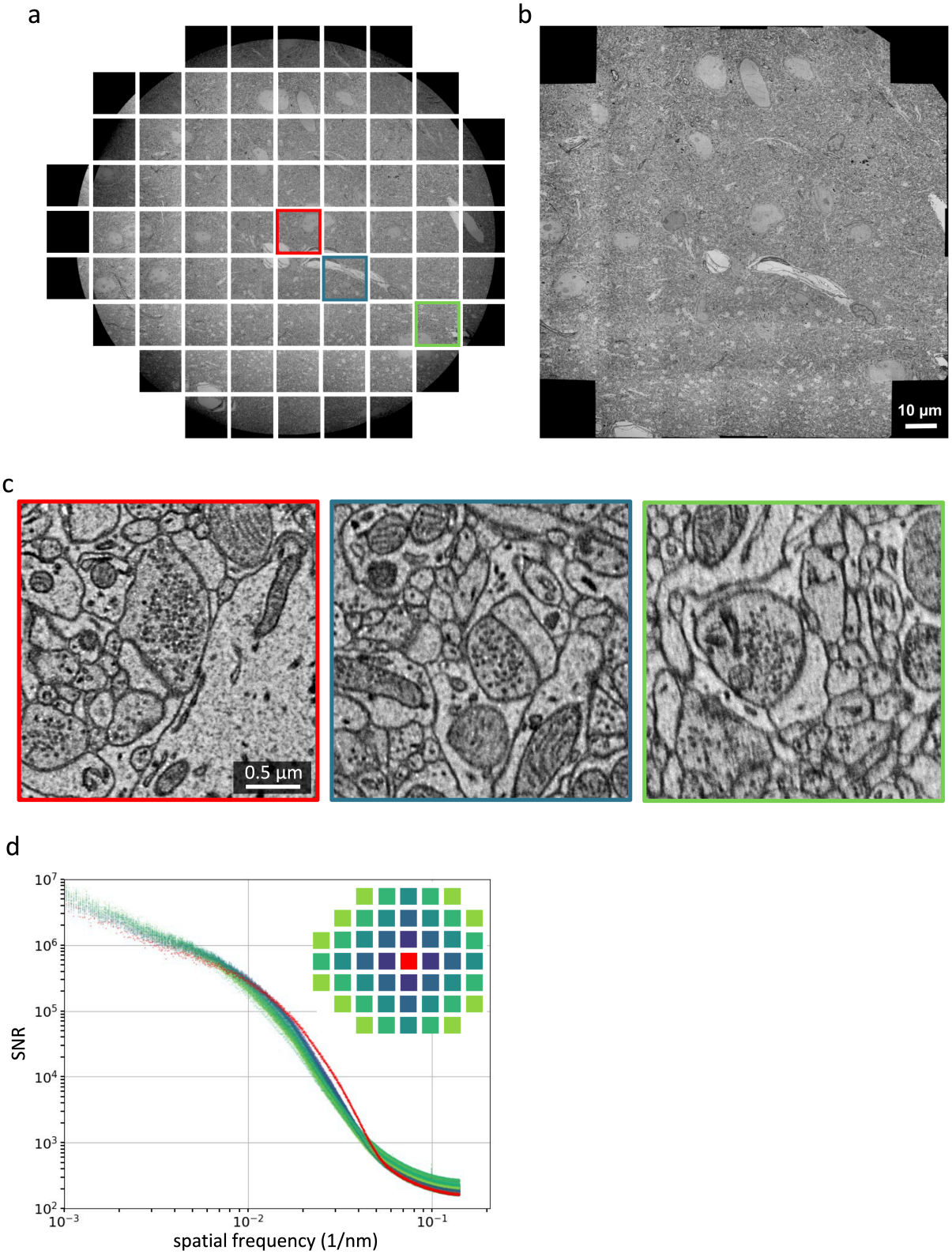

Fig. 3

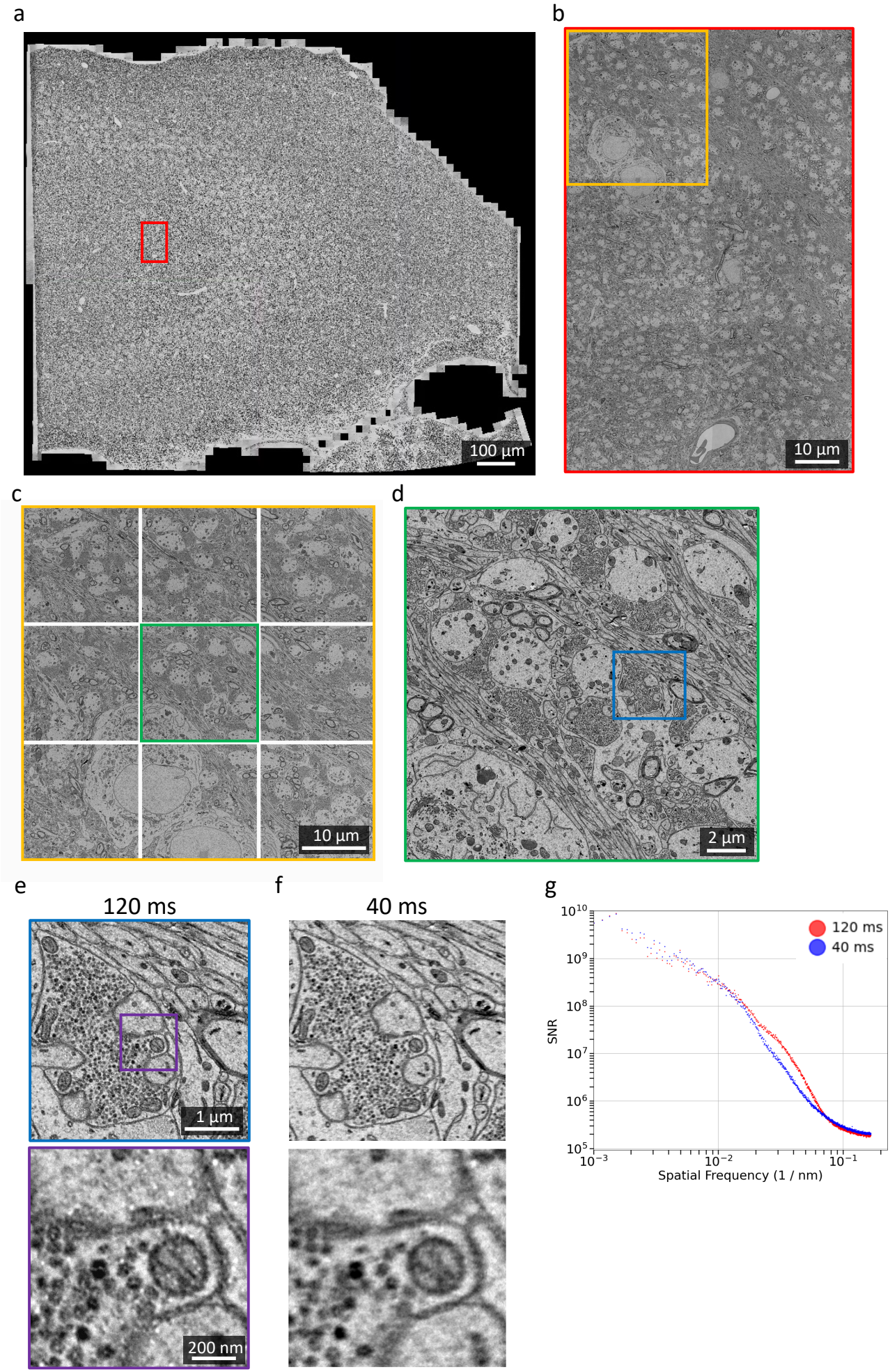
a
100 µm
b
10 µm
c
10 µm
d
2 µm
e
120 ms
1 µm
200 nm
f
40 ms
g
120 ms
40 ms
SNR
Spatial Frequency (1 / nm)

Fig. 4

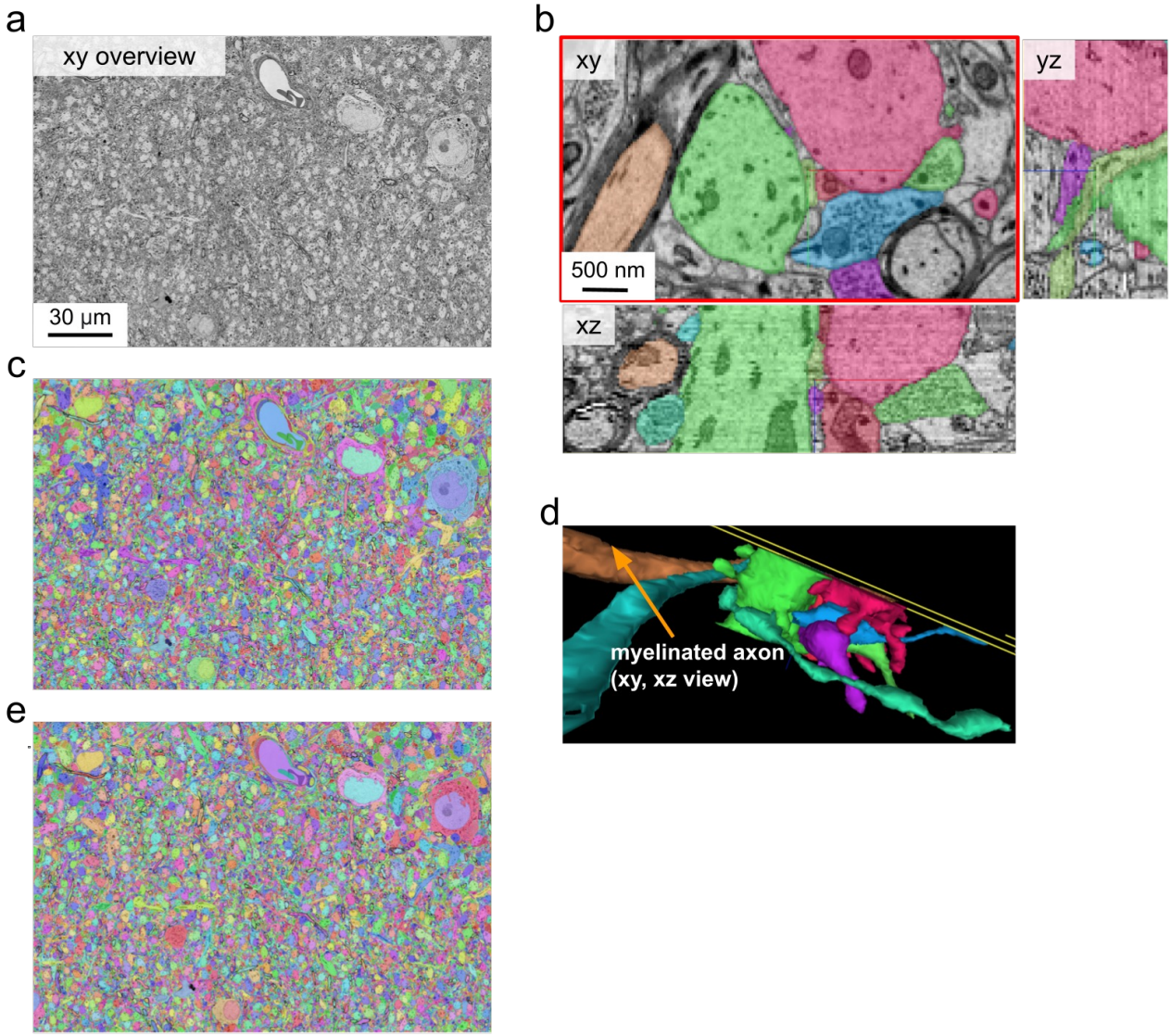
a
xy overview
30 µm
b
xy
500 nm
yz
xz
c
d
myelinated axon
(xy, xz view)
e

Table 1

Performance metric for TEM with Cricket (1 mm² section of 45 nm thick)					
imaging parameters	avg 3 nm/pix (120 ms exp.)	avg 3 nm/pix (40 ms exp.)	peak 3 nm/pix (40 ms exp.)	avg 3.6 nm/pix (40 ms exp.)	unit
x,y resolution*	3	3	3	3.6	nm/pixel
tile size	6000	6000	6000	6000	pix (aspect ratio of 1:1)
FOV size	18	18	18	21.6	µm
pixels per tile	36	36	36	36	Mpixel
supertile size (per side, 15% overlap b/w tiles)	16200	16200	16200	16200	pix (aspect ratio of 1:1)
overlap between supertiles	600	600	600	600	pix (i.e. 10% of tile size)
exposure time	120	40	40	40	ms
tiles per section (w/ overlap)	4356	4356	4140	2916	tile
supertiles per section (w/ overlap)	484	484	460	324	supertile
imaging time per section	11.7	6.6	4.7	4	minute
transition overhead (tape translation, ROI, autofocus, etc.)	2.2	2.2	1.8	2.2	minute
total time per section	13.9	8.8	6.5	6.2	minute
burst imaging rate (imaging only)	300	900	900	900	Mpix/s
section imaging rate (w/ stage, Cricket)	223	397	529	437	Mpix/s
net imaging rate (w/ stage, Cricket, transition)	188	297	382	282	Mpix/s
effective imaging rate (w/ stage, Cricket, transition, overlap)	142	224	288	213	Mpix/s
sections per day (1 scope at 24 hr)	103	163	221	232	section
time to image 1 mm³ (4 scopes at 24/7)	54	35	26	24	days
time to image 1 mm³ (4 scopes at 65% uptime #)	83	53	39	37	days
# 65% uptime accounts for microscope maintenance, imaging pause (Yin et al. 2020)					
*Typical z resolution (section thickness) for TEM is 45 nm, while FIB-SEM offers a z resolution of up to 4 nm (Xu et al. 2017).					